Journal of Magnetic Resonance **142,** 207–215 (2000)
doi:10.1006/jmre.1999.1916, available online at http://www.idealibrary.com on IDEAL®

Microscopic Displacement Imaging with Pulsed Field Gradient Turbo Spin–Echo NMR[1]

T. W. J. Scheenen, D. van Dusschoten, P. A. de Jager, and H. Van As[2]

Laboratory of Molecular Physics, Department of Biomolecular Sciences, Wageningen University, Dreijenlaan 3, 6703 HA Wageningen, The Netherlands

Received January 19, 1999; revised August 18, 1999

We present a pulse sequence that enables the accurate and spatially resolved measurements of the displacements of spins in a variety of (biological) systems. The pulse sequence combines pulsed field gradient (PFG) NMR with turbo spin–echo (TSE) imaging. It is shown here that by ensuring that the phase of the echoes within a normal spin–echo train is constant, displacement propagators can be generated on a pixel-by-pixel basis. These propagators accurately describe the distribution of displacements, while imaging time is decreased by using separate phase encoding for every echo in a TSE train. Measurements at 0.47 T on two phantoms and the stem of an intact tomato plant demonstrate the capability of the sequence to measure complete and accurate propagators, encoded with 16 PFG steps, for each pixel in a 128 × 128 image (resolution 117 × 117 × 3000 μm) within 17 min. Dynamic displacement studies on a physiologically relevant time resolution for plants are now within reach.

Key Words: **flow; diffusion; transport processes; plants; porous systems.**

INTRODUCTION

Diffusion and transport processes of water in objects such as tissues, soils, model systems, plants, food, separation columns, bioreactors, and biofilms are of interest for researchers in many different fields. Some problems can arise when complex porous systems such as vegetable or animal tissues are monitored: the water status of the studied system can change quickly, and water flow profiles and diffusional properties (e.g., restrictions) are generally unknown. Dynamic NMR microscopy (*2*) provided the means to study the distribution of water displacements microscopically and noninvasively in a wide variety of systems. This method combines NMR imaging with quantitative displacement studies using pulsed field gradients (PFGs).

Since the water status of a plant can change within half an hour, dynamic studies of that status should be at a physiologically relevant time scale of less than 20 min. Because the flow profile and diffusive behavior of the plant tissue are not known, a complete distribution of displacements within a certain time must be constructed for every pixel of an image and the SNR of the properties of interest must be sufficiently high to produce results with acceptable accuracy. The standard dynamic NMR experiment, in which an image with $n \times n$ picture elements is recorded, combined with m gradient steps to encode for displacement takes $n \times m$ acquisitions to complete. Consequently, the total acquisition time may exceed several hours (*3, 4*), and changes within the measurement time will be averaged out over the experiment. Therefore, a faster way of performing the dynamic NMR experiment is needed in plants.

The time resolution of a PFG NMR imaging experiment can be increased by reducing the number of phase and flow encoding steps (*5, 6*). Reducing the number of phase encoding steps directly reduces the spatial resolution in one direction of the images, which is not desirable in plants, where the small tissue dimensions require an in-plane resolution on the order of 100×100 μm. Rokitta *et al.* (*6*) assumed a certain flow profile for the observed spins and fitted the signal, attenuated by a reduced number of flow encoding steps, to a model function. Another approach to decrease measurement time is the use of an echo train. Echo planar imaging (EPI, (*7, 8*)) is not applicable in plants, because intercellular spaces in plant tissues cause magnetic field gradients in the sample and shorten the T_2^* drastically (e.g., $<$40 ms). In a 180° pulse train with normal spin echoes, the signal decays under the influence of the longer T_2. The multiple spin echoes can be used to step rapidly through k space by phase encoding the echoes separately (turbo spin echo, TSE or RARE (*9*)). TSE is used here with the new feature that all echoes in the train can be acquired with constant and coherent amplitude and phase, which is a prerequisite for combining dynamic NMR microscopy with TSE. Thus not only the signal amplitude attenuation can be measured as a function of the PFGs (*10*) but also the phase development, containing flow information.

THEORY

The displacement of an ensemble of spins in a magnetic field can directly be measured by the use of two gradient pulses **g** of duration δ and spacing Δ (see Fig. 1). A uniform displacement **R** of the spins results in a phase shift ϕ of the NMR signal:

[1] Parts of this work were presented at the Fourth International Conference on Magnetic Resonance Microscopy and Macroscopy in Albuquerque, NM, on Sept. 20–24, 1997 (*1*).

[2] To whom correspondence should be addressed. E-mail: Henk.Vanas@water.mf.wau.nl.

1090-7807/00 $35.00

$$\phi = \gamma\delta\mathbf{g}\cdot\mathbf{R}, \qquad [1]$$

in which γ is the gyromagnetic ratio of the spins observed.

If the displacement of the spins within the observation time Δ is not uniform but completely random, e.g., diffusion in a nonflowing liquid with a self-diffusion constant D, there will be no phase shift but only an attenuation of the NMR signal amplitude $S(\mathbf{g})$ vs $\mathbf{g}$ normalized to the signal amplitude $S(0)$ at $\mathbf{g} = 0$ (*11*):

$$S(\mathbf{g})/S(0) = \exp(-\gamma^2\mathbf{g}^2\delta^2 D(\Delta - \delta/3)). \qquad [2]$$

If the displacement behavior of the ensemble of spins under observation is known *a priori*, e.g., for pure uniform diffusion or plug flow, an experiment with two $\mathbf{g}$ values ($\mathbf{g} = 0$ and $\mathbf{g} = x$) would be enough to determine the flow velocity and the diffusion constant of the spins. Quantification problems emerge if the displacement behavior of individual spins in the ensemble is not known. Experiments with two $\mathbf{g}$ values can only result in one weighted mean flow velocity or diffusion coefficient (*12–17*).

As soon as a biological system is studied, multiple spin ensembles that differ in diffusion constants and flow velocities contribute to the NMR signal both in spatially unresolved measurements and even in individual pixels of a high-resolution image. To correctly quantify the unknown displacement behavior of the observed ensemble of spins, one must measure the NMR signal $S(\mathbf{g})$ as a function of $\mathbf{g}$ (*18*). In that case, the NMR signal is a superposition of phase terms $\exp(i\gamma\delta\mathbf{g}\cdot(\mathbf{r}' - \mathbf{r}))$ derived from Eq. [1] weighted with the spin density $\rho(\mathbf{r})$ at a position $\mathbf{r}$ multiplied by the probability $P(\mathbf{r}|\mathbf{r}', \Delta)$ that a spin moves from position $\mathbf{r}$ to position $\mathbf{r}'$ in time Δ:

$$S(\mathbf{g}) = \int \rho(\mathbf{r}) \int P(\mathbf{r}|\mathbf{r}', \Delta)\exp(i\gamma\delta\mathbf{g}\cdot(\mathbf{r}' - \mathbf{r}))d\mathbf{r}'\, d\mathbf{r}. \qquad [3]$$

By defining a reciprocal space $\mathbf{q} = \gamma\delta\mathbf{g}/2\pi$ and a dynamic displacement $\mathbf{R} \equiv \mathbf{r}' - \mathbf{r}$, independent from the initial spin position and density, one can rewrite Eq. [3] as

$$S(\mathbf{q}) = \int \bar{P}(\mathbf{R}, \Delta)\exp(i2\pi\mathbf{q}\cdot\mathbf{R})d\mathbf{R} \qquad [4a]$$

$$\bar{P}(\mathbf{R}, \Delta) = \int S(\mathbf{q})\exp(-i2\pi\mathbf{q}\cdot\mathbf{R})d\mathbf{q}. \qquad [4b]$$

This demonstrates the Fourier relationship between $S(\mathbf{q})$ and $\bar{P}(\mathbf{R}, \Delta)$. A Fourier transform of $S(\mathbf{q})$, the NMR signal as a function of $\mathbf{q}$, results in the averaged probability distribution of displacements of all spins observed: the averaged propagator, $\bar{P}(\mathbf{R}, \Delta)$.

The mean square displacement σ^2 due to (unrestricted) diffusion is proportional to the corrected observation time ($\Delta - \delta/3$) and results in a Gaussian propagator positioned at the mean displacement p of the observed water molecules:

$$\bar{P}(\mathbf{R}) = A\exp\left(-\left(\frac{R - p}{\sigma}\right)^2 \Big/ 2\right). \qquad [5]$$

For stationary water the mean displacement is zero, resulting in a Gaussian distribution of $\bar{P}(\mathbf{R})$ with amplitude A and center position $p = 0$. The mean square displacement σ^2 can be used to calculate the diffusion coefficient of the water through

$$\sigma^2 = 2D(\Delta - \delta/3). \qquad [6]$$

The probability distribution function for water flowing laminarly through a tube is the unit step function

$$\bar{P}(\mathbf{R}) = C \quad \text{for } 0 < \mathbf{R} < \mathbf{R}_{max}$$
$$\bar{P}(\mathbf{R}) = 0 \quad \text{for } \mathbf{R} < 0 \text{ and } \mathbf{R} > \mathbf{R}_{max}, \qquad [7]$$

where C is a constant and $\mathbf{R}_{max}$ is the maximum displacement of the water in the tube within Δ. Since flowing water also exhibits diffusion, the unit step function is broadened and the borders at $\mathbf{R} = 0$ and $\mathbf{R} = \mathbf{R}_{max}$ appear as half-Gaussians instead of sharp edges of the propagator.

When q-space imaging is combined with normal NMR imaging, one can perform so-called dynamic microscopy experiments, a term which was first named by Callaghan (*2*).

In conventional imaging, the signal in time t evolves under the influence of a gradient G encoding for position (in two dimensions). Diffusion and flow in the direction of the imaging gradients might introduce extra signal attenuation if the imaging gradients are of significant size compared to the PFGs. However, this extra signal attenuation, if any, will not vary as a function of the PFGs but will be equal for every step in q space. Therefore the imaging gradients will not affect the shape of the propagator. So incorporating the well-known k-space description for imaging

$$S(\mathbf{k}) = \int \rho(\mathbf{r})\exp(i2\pi\mathbf{k}\cdot\mathbf{r})d\mathbf{r}, \qquad [8]$$

with $\mathbf{k} = \gamma\delta\mathbf{G}/2\pi$ in Eq. [4] the total signal as a function of k and q space is

$$S(\mathbf{k}, \mathbf{q}) = \int \rho(\mathbf{r})\exp(i2\pi\mathbf{k}\cdot\mathbf{r}) \int \bar{P}(\mathbf{R}, \Delta) \times \exp(i2\pi\mathbf{q}\cdot\mathbf{R})d\mathbf{R}\, d\mathbf{r}. \qquad [9]$$

The result of such a microscopic displacement measurement is a series of conventional images, obtained after a two-dimensional Fourier transform with respect to **k**, which contains the propagator of the spins after Fourier transform with respect to **q** in the third dimension.

MATERIALS AND METHODS

The Pulse Sequence

Figure 1 shows an outline of the pulsed field gradient turbo spin–echo (PFG-TSE) pulse sequence. This sequence is a combination of two techniques: the pulsed field gradient Carr–Purcell (PFG CP) sequence (*19*) and the turbo spin–echo technique, also known as RARE (*9*), originating from the idea of using multiple echoes to phase encode the NMR signal (*7*). The improvement of this sequence compared to previous reports on PFG-TSE (*10*) involves the ability to maintain a constant amplitude and phase throughout the echo train. This is the property that enables the combination of encoding for flow with PFGs and decreasing the acquisition time with the TSE technique. A short description of the sequence follows.

In the first part of the sequence a selective 90° pulse induces magnetization perpendicular to the static magnetic field in a selected slice. This magnetization is encoded for displacement by two ramped PFGs in the slice direction. The amplitude of **g** is varied from $-g_{\max}$ via zero to $+g_{\max-1}$ in m steps. In calculating the effective duration δ of a PFG, one ramp is included. Δ can be varied by changing the first echo time t_e1 and additional 180° pulses with variable spacing τ (*20*) can be inserted between the two PFGs. The signal is not stored along the z axis during $\Delta - \delta$ as in a stimulated echo (STE) sequence (*21, 22*) but remains in the xy plane. In the xy plane the additional 180° pulses are used to overcome susceptibility problems by refocusing the signal. The XY-8 phase scheme $(xyxyyxyx)_n$ is used to avoid losing the phase dispersion imposed by the first PFG in the time between the two PFGs due to RF pulse imperfections (*19, 20*).

In the second part of the sequence the displacement-encoded complex NMR signal is phase sensitively recorded in a train of spin echoes. The cumulative error of imperfect 180° pulses is now overcome by using an MLEV-4 $(x\text{–}x\text{–}x\ x)_n$ phase pattern in the pulse train, which performed best with the instrumental setup used (*23*). The use of spin echoes compared to gradient echoes has the advantage that the decay in signal amplitude of the echoes in the train is governed by T_2 instead of T_2^*, which is the case in an EPI experiment (*12, 15*). This advantage turns into an absolute necessity if samples with very short T_2^* values are studied. The susceptibility problems in plants can only be overcome by using a spin–echo train. The combination of short, hard 180° pulses (24 μs) and strong, fast switching gradients (100 μs ramps) enables short echo times (4.60 ms) at a spectral width of 50 kHz and 128 sample points. The receiver acquires data with a high duty cycle (2.56 ms acquisition in every 4.60 ms echo). The signal attenuation due to the short T_2^* is negligible compared to the controlled signal attenuation resulting from the high read-out gradient to ensure that the observed resolution of the image is the same as the calculated resolution (*24, 25*).

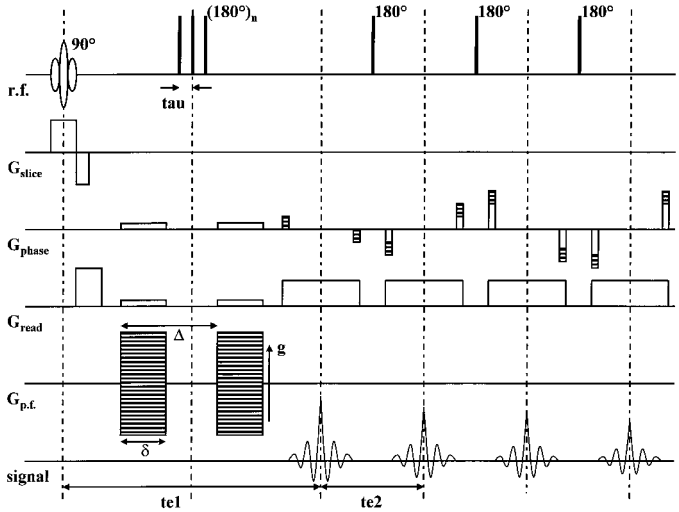

FIG. 1. Pulsed field gradient turbo spin–echo pulse sequence. All directions show a pair of crusher gradients around the first (train of) 180° pulse(s). In the direction of the displacement-encoding PFGs (the slice direction), the crushers are negligible compared to the PFGs.

The number of echoes in the RF pulse train used for phase encoding the NMR signal (the turbo factor tf) is variable and is determined largely by the T_2 of the sample. Figure 2 shows the k-space raster for an experiment in which eight scans with 32 echoes form two images. The center of k space, around $k_y = 0$, is sampled with the first two echoes of the eight scans. All subsequent echoes are placed symmetrically around $k_y = 0$. In this way, the T_2 relaxation in the echo train leads to a stepped decrease of the signal amplitude in k space from $k_y = 0$ to the borders of k_y. The choice in the number of echoes is a compromise between measurement time and resolution. If too many echoes are used, the signal of those pixels with short T_2 values decays too much, resulting in a heavy filtering in the k_y direction: the intensity of the pixel containing water with the short T_2 values is distributed over neighboring pixels in the phase-encoding direction. Different trajectories through the k_y direction should minimize this artificial spreading (*26*). Furthermore, to reduce unwanted recombination of phase-encoding gradients, every echo is phase encoded differently from its neighboring echoes. This is possible by rewinding the phase gradient after each echo (*27*).

It should be noted that the phase of the odd and even echoes is not exactly the same but remains constant for both types of echoes throughout the echo train. Therefore the odd and even echoes are separately phase encoded to form two completely separate images (see k-space trajectory in Fig. 2). Using, for example, a tf of 32 means that for images of n^2 pixels $2n$/tf scans are acquired in which 16 odd and 16 even echoes are used for phase encoding the signal, resulting in two n^2 complex

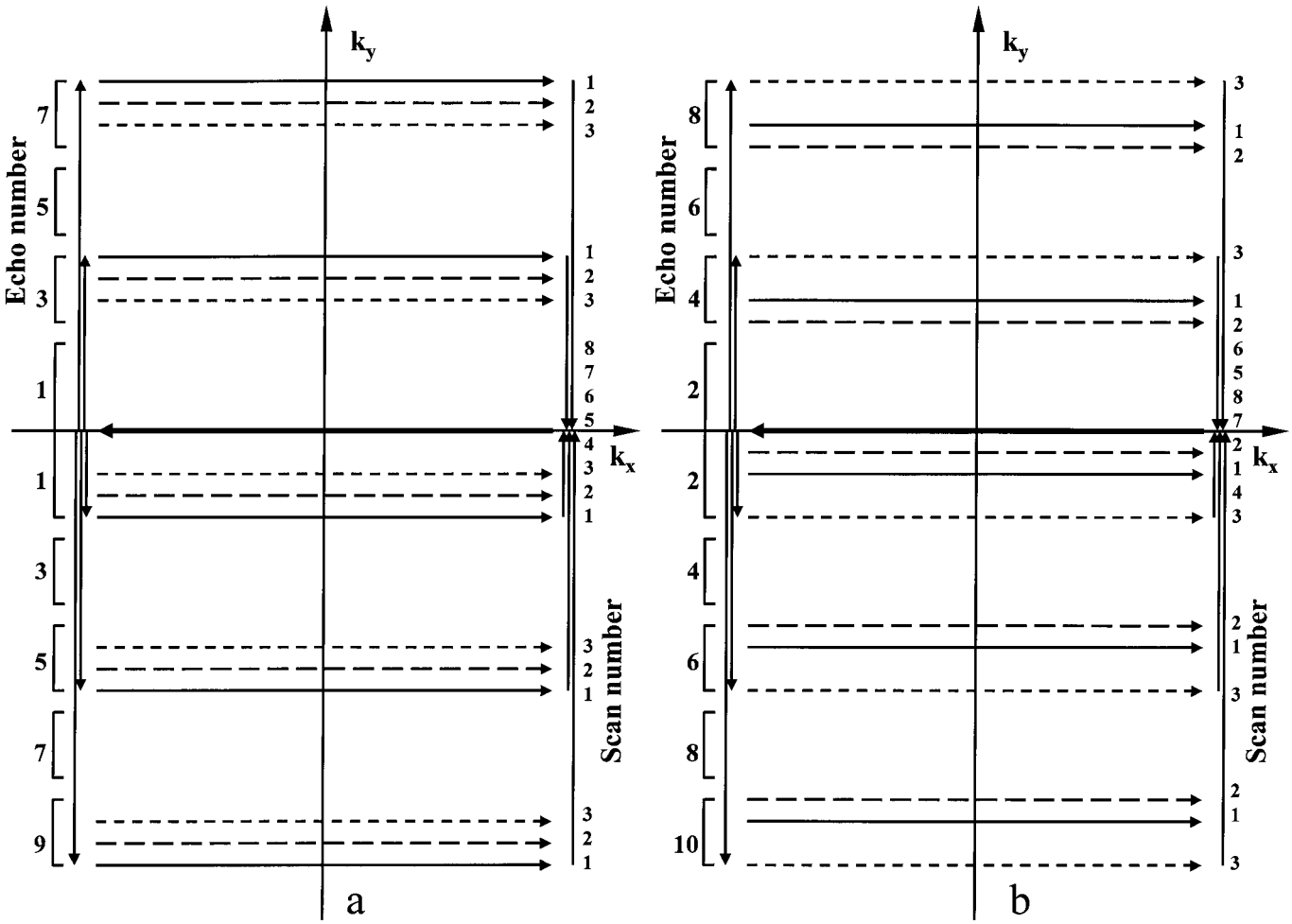

FIG. 2. *k*-space raster for a 128 × 128 image obtained in eight scans. The first echoes of the eight scans form the center of *k* space for the odd-echo image (a), and the second echoes of the eight scans form the center of *k* space for the even-echo image (b). The third and all other odd echoes are placed symmetrically around the center of the *k*-space raster for the odd-echo image, just like the fourth and further even echoes are placed symmetrically around the center of the *k*-space raster for the even-echo image.

images: one from the even and one from the odd echoes. After phase correction, the two complex images are summed to increase the SNR.

In the first and second parts of the sequence, hard 180° pulses are used, since they are short. Residual magnetization of the hard pulses in the *xy* plane is suppressed with gradients: crusher pairs are applied in three directions. In the direction of the displacement-encoding PFGs, the crushers are of negligible size compared to the PFGs. The dephasing read-out gradient is applied before the first 180° pulse, so refocusing of initial magnetization of the soft 90° pulse will not occur at the same time as any residual magnetization from the hard pulses in the read-out direction. A disadvantage of using hard 180° pulses instead of soft pulses in combination with slice gradients is that the time between scans cannot be used to measure a different slice, because the whole sample is excited with the pulses. A multislice experiment is still possible but requires measurement conditions (longer echo times or larger spectral width) different from those of a single-slice experiment (*28*).

If averaging is necessary to increase the SNR of the images, dc artifacts are subtracted by taking an even number of averages in which the phase of the soft 90° pulse is shifted by π for every scan. If averaging is not performed, a dc correction is made by subtracting the mean level where no signals are present from the echoes.

Measurement Objects and Spectrometer

Three objects were used to test and illustrate the possibilities of the pulse sequence: two phantoms and a tomato plant. The first phantom consisted of six small test tubes filled with water, doped with different concentrations of $MnCl_2$ to vary the T_2. This was done to study the effect of the different T_2 values on the quality of the TSE images and the effect on the single-pixel propagators. The second phantom, used to evaluate the accuracy of measuring flow with the PFG-TSE imaging sequence, was a test tube (i.d. 3.0 cm) filled with doped water (tap water with $CuSO_4$). Inside the test tube with stationary water was a

TABLE 1

Mean Values and Standard Deviations (SD) of the Following Calculated Parameters for the Six Different Tubes in the First Phantom: The T_2, the Signal Amplitude at the Moment of Excitation (Amp), the Self-Diffusion Constant in the Propagator (D_1), and the Self-Diffusion Constant in the Stejskal–Tanner Plot (D_2)

Tube	$[MnCl_2]$ (mmol/L)	T_2 (ms)	SD (ms)	Amp (au)	SD (au)	D_1 (10^{-9} m^2/s)	SD (10^{-9} m^2/s)	D_2 (10^{-9} m^2/s)	SD (10^{-9} m^2/s)
I	0.0	1.5×10^3	4.5×10^3	10.2	0.6	2.20	0.16	2.20	0.19
II	0.2	118	3	25.8	1.1	2.19	0.13	2.24	0.13
III	0.4	59.8	2.1	26.1	1.1	2.18	0.18	2.27	0.17
IV	0.8	29.2	1.3	24.6	1.4	2.23	0.13	2.37	0.22
V	2.5	8.3	1.7	22.7	1.8	2.18	0.16	2.30	0.30
VI	5.0	5.4	0.5	23.8	3.4	2.08	0.29	1.97	0.40

second, empty test tube and a third, flexible, looped tube with water passing through the RF coil two times: flowing up and down. The flow rate through the flexible tube was controlled with a Waters 4000 HPLC pump (Waters Corp., Milford, MA).

The final object was a 60 cm tall, 10 week old, tomato plant. The plant, including pot, was put in the instrumental setup (light intensity approximately 150 lux, relative humidity 65%, and air temperature 26°C) 2 days before measurements and was flowering during the measurement.

The spectrometer was an SMIS console (SMIS Ltd., Guildford, Surrey, UK), operating at 20.35 MHz, equipped with an electromagnet (Bruker, Karlsruhe, Germany), which generates the 0.47 T field over a 14 cm air gap and is stabilized by the use of an external ^{19}F lock unit (SMIS). The phantoms and the tomato plant were measured in a custom-engineered gradient and RF probe (Doty Scientific Inc., Columbia, SC) with a 45 mm (i.d.) cylindrical central bore, accessible from both ends. The 48 mm solenoid RF coil was surrounded by a set of actively shielded gradients (maximum strengths were 0.60, 0.51, and 0.60 T/m for the x, y, and z directions, respectively). For the measurements on the tomato plant, the probe's RF coil was detuned and an extra solenoid RF coil with an i.d. of 15 mm, directly wrapped around the plant stem, was inserted in the 45 mm bore gap of the gradient probe, increasing the SNR by a factor of approximately 48/15 $\approx$ 3 (*29*).

Signal Processing

A data set of m images with n^2 pixels obtained with the PFG-TSE pulse sequence contains three dimensions of complex data. The first dimension contains n sample points in which one echo is read out. The second dimension is composed of a number of views ($2n$/tf) and echoes (tf), which are necessary to form the total of n phase-encoding steps for two images. The third dimension holds the m PFG steps. The primary data handling involves reshuffling the different views and echoes into n phase-encoding steps for two images in the correct order with respect to k_y. The complex k-space data is Fourier transformed and here the main reason for obtaining two complete complex images emerges: the image constructed from the odd echoes is shifted slightly in the phase-encoding direction (less than one pixel) with respect to the image of the even echoes. A first-order phase correction in the phase-encoding direction before the Fourier transform minimizes the difference in position of the sample in the two images.

Subsequently, zero- and first-order phase corrections of the even and odd echo images at $\mathbf{g} = 0$ are performed in both image directions and used to correct the displacement-encoded images. Furthermore, a linear phase shift of the total images with respect to $\mathbf{g}$ is caused by a PFG-dependent B_0 field shift and is corrected by zeroing the phase of stationary water either in a reference tube or in the studied object. Finally, the PFG direction or q-space data are zero filled once and Fourier transformed to form a complex propagator for every pixel in the even and odd images. The propagators of the odd images are mirrored and shifted by one point to enable the addition of the odd and even images to one final image set (so-called propagator images). The real part of this set contains the propagators whereas the imaginary part only contains noise. The width of the displacement axis of the propagator is determined by $1/\gamma g_{step}\delta$. In the 3D FT no filtering is applied. All data handling is performed in IDL (RSI, Boulder, CO).

RESULTS

The Phantoms

The T_2 values of the six test tubes in the first phantom varied over a range of three decades. To measure these T_2 values, we used a multiecho experiment with a train of 48 echoes (echo time $n \times 4.6$ ms) to obtain a series of images with decreasing intensity. For every pixel in the images the real part of the complex signal attenuation (after phase correction) in the echo train was fitted to a monoexponential decay to calculate values for T_2 and the initial signal amplitude (*23*). Table 1 contains the calculated values of mean T_2 and initial signal amplitude together with standard deviations for every tube: T_2 values range from 5.4 ms to 1.5 s. The mean signal amplitude for every tube was calculated from only those pixels (around 45 for every tube) that were completely filled with water: we did not use pixels near edges to exclude partial volume effects.

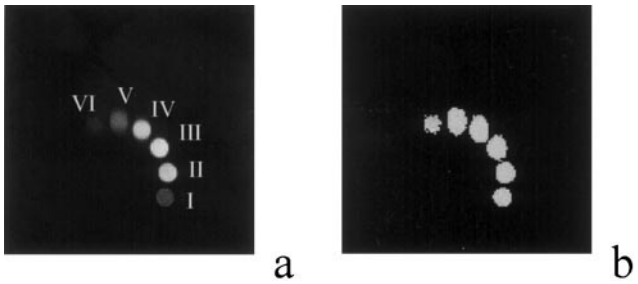

FIG. 3. Images of six tubes with doped water: (a) the real part of the complex signal at $\mathbf{g} = 0$ of a PFG-TSE experiment; (b) D for every pixel, calculated through Eq. [5], with σ derived from the fit to the propagator. Parameters: image size 128 × 128 pixels, field of view (FOV) 55 mm, t_e1 13.0 ms, t_e2 4.6 ms, Δ 6.26 ms, δ 3.5 ms, tr 480 ms, slice thickness 3 mm, 16 PFG steps, PFG_{max} 0.457 T/m, tf 16, measurement time 4 min 23 s, T 24°C.

Since partial volume effects do not significantly influence signal attenuation, we did use partially filled pixels to calculate T_2 values; for the mean T_2 values, around 80 pixels were used for calculations. In the calculated mean amplitudes the amplitudes of tubes II to VI are comparable. Only tube I shows a lower amplitude, because of partial saturation: the low signal intensity and the long T_2 (and therefore long T_1) compared to tr result in an inaccurate estimation of T_2 and an underestimated calculated amplitude (see Table 1).

Figure 3a shows an image of the same six tubes filled with doped water, acquired with the PFG-TSE sequence at $\mathbf{g} = 0$. Although the first echo in the experiment is at 13.0 ms after excitation, one can still observe tube VI with a T_2 of 5.4 ms. The effect of smearing of these short T_2 values in the vertical, phase-encoding direction of the images is clear in tubes V and VI and some vertical ghosting is present around tubes IV and V (maximum intensity around 7% of maximum intensity in the tube). Subsequently, we obtained propagator images for the six phantom tubes and subjected all propagators to a nonlinear least-squares fit to a Gaussian function (Eq. [5]) using the Levenberg–Marquardt method (*30*). To calculate the diffusion constant D from σ, we used Eq. [6]. These results are presented in Fig. 3b. The data from the PFG-TSE experiment were also analyzed in the same manner as proposed by Stejskal and Tanner (Eq. [2], (*11*)): a weighted least-squares linear fit of $\ln(S(g)/S(0))$ to $\gamma^2\mathbf{g}^2\delta^2(\Delta - \delta/3)$ for every pixel resulted in a D map. The mean D and its standard deviation (SD) for each tube in the images is summarized in Table 1. We take 2.20×10^{-9} m^2/s to be the self-diffusion constant D for free water.

Propagator images of the second phantom (Fig. 4a) were fitted to Eq. [5]. The propagators of three pixels (solid lines)—one pixel with stationary water, one pixel in the middle of the tube with water flowing up, and one pixel in the middle of the

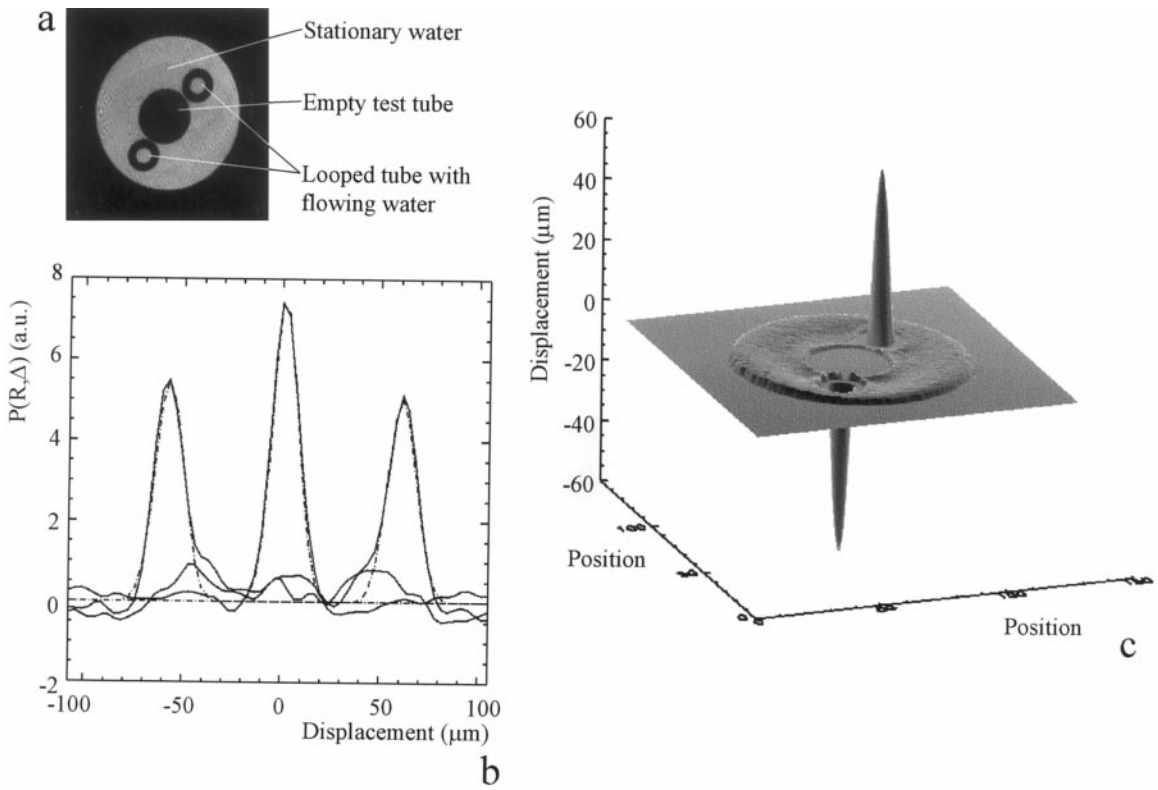

FIG. 4. Summary of data of the phantom with stationary and flowing water. (a) An image at $\mathbf{g} = 0$, perpendicular to the axes of the tubes. (b) The propagators of three individual pixels (solid lines) and their fits to the Gaussian function (dashed line). One pixel contains stationary water, one pixel has maximum flow up, and one pixel has maximum flow down through the slice. (c) Mesh plot of the spatial distribution of displacements. The countercurrent flow of water results in two antisymmetrical parabolic profiles in the tube with flowing water. Parameters: FOV 40 mm, t_e1 20.2 ms, t_e2 4.8 ms, Δ 12.76 ms, δ 4.5 ms, tr 1700 ms, slice thickness 3 mm, 32 PFG steps, PFG_{max} 0.385 T/m, tf 32, measurement time 16 min 30 s, T 24°C, volume flow 1.00 ml/min.

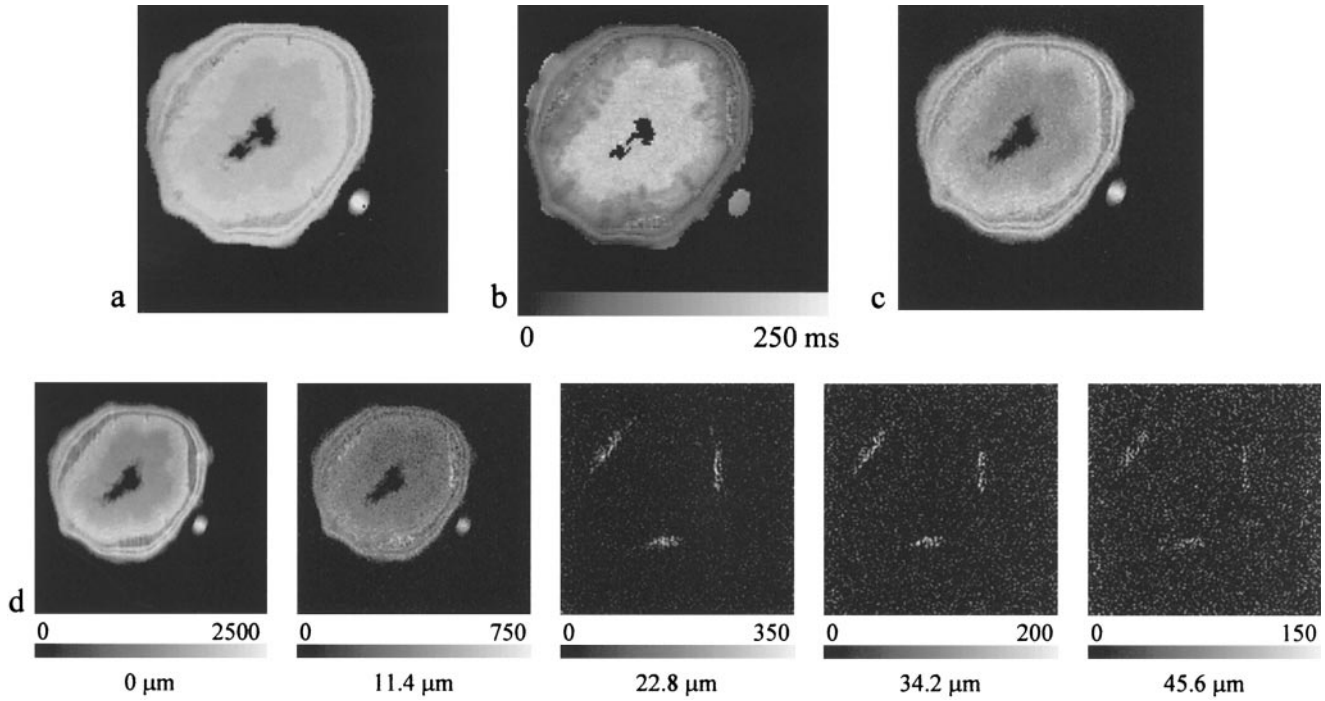

FIG. 5. Images of a transverse slice through the stem of the tomato plant. (a) A calculated amplitude image. (b) A calculated T_2 image. (c) A TSE image at $\mathbf{g} = 0$ of the real signal amplitude after phase correction. (d) Images of the real signal amplitude at calculated displacements of 0, 11.4, 22.8, 34.2, and 45.6 μm. The shown signal intensities are in arbitrary units. Parameters for (a) and (b): FOV 14 mm, t_e1 8.6 ms, t_e2 5.2 ms, tr 1500 ms, slice thickness 3 mm, acquisition time 32 min, T 26°C. Extra parameters for (c) and (d): FOV 15 mm, t_e1 17.2 ms, Δ 9.56 ms, δ 4.5 ms, tr 800 ms, 16 PFG steps, PFG_{max} 0.457 T/m, tf 32, measurement time 17 min 8 s.

tube with water flowing down—with their fits (dashed lines) to the Gaussian function are displayed in Fig. 4b. Since displacement caused by coherent flow is proportional to Δ, the position p of the fit to the Gaussian function corresponds to the mean displacement of the water in the observed pixel within Δ. Figure 4c displays p for every individual pixel of the slice through the phantom. The maximum displacement of the water flowing up and down through the slice was measured at 60.8 and 58.9 μm within Δ, respectively. These values correspond to linear flow velocities of 4.76 and 4.62 mm/s. The forced water volume flow of the pump was set to 16.7 mm^3/s, which, assuming a laminar, parabolic flow profile exists within the tube (i.d. 3.0 mm), results in a maximum linear velocity of 4.72 mm/s.

Additionally, Eq. [1] predicts a linear relation between the phase of the NMR signal and the displacement of the spins in time Δ. When the phase of the signal of the center of the tubes was fitted to Eq. [1], we found a maximum linear velocity of 4.81 mm/s (flowing up) and 4.52 mm/s (flowing down). The correct value should be 4.72 mm/s, as reported earlier.

The Tomato Plant

The most demanding object in terms of time resolution and spatial resolution, but also the most interesting object in terms of dynamics presented here, is the stem of a tomato plant. Figures 5a and 5b show single-parameter images of the amplitude and T_2 of the stem of the tomato plant, acquired in the same manner as described for the first phantom. The TSE image at $\mathbf{g} = 0$ is shown in Fig. 5c. One can observe that the stem mainly consists of spongy parenchyma with large cells, which results in high values for T_2. In the center of the stem a cavity is visible where no signal is detected. The outer rings of the stem, from the ring with lower intensity near the middle and three broadened regions visible in the amplitude image, up to the surface of the stem contain transport vessels with supporting tissues and fibers. T_2 values in the outer rings show more diversity because of the different cell structures and sizes (*31*) which occur there. The dot on the lower right side of the images is a reference tube with doped water. The reference tube axis is not exactly perpendicular to the image plane so its image is somewhat elliptical.

The pixel size of this image set containing the single pixel propagators is 117 $\times$ 117 $\times$ 3000 μm. From microscopic studies, we know that the internal diameters of the xylem vessels in the stem range from approximately 10 to 160 μm (*32*). Distances between individual xylem vessels are in the same order of magnitude.

Since most xylem vessel radii are smaller than the pixel size, there will probably be no pixels in the images that contain only flowing water. From the information contained in the propagator images, images can be constructed representing the prop-

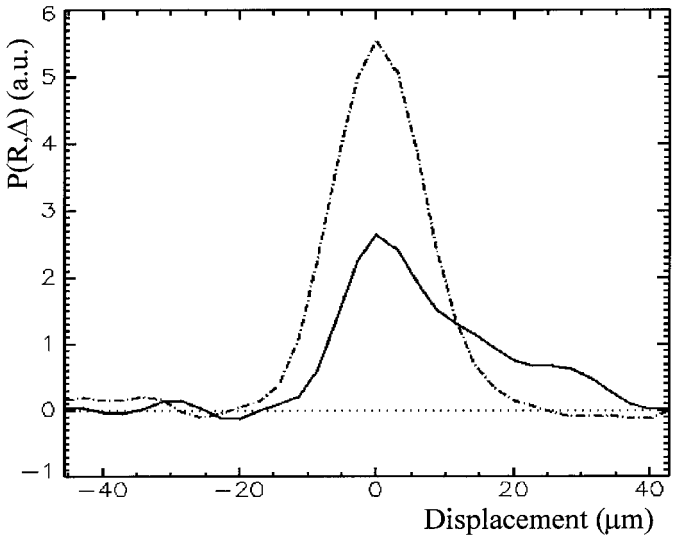

FIG. 6. Propagator of a pixel in the reference tube (dashed line) and a pixel in one of the three areas of the tomato plant that show flow (solid line).

agator intensity for a certain displacement. A series of such images (Fig. 5d) gives an overview of the water displacement in the slice. In this way, one can detect three areas with pixels with low amplitudes at 0 μm displacement but high intensity at larger displacement. The pixels in these areas resemble volume elements in which water is transported upward in the plant and they coincide with the regions with active xylem vessels of the tomato plant (*32*).

The propagator of one pixel in the active xylem area is displayed in Fig. 6, together with the propagator of a pixel in the reference tube. The propagator of the pixel in the xylem area shows displacements within Δ up to 30 μm, which corresponds to a flow velocity of 3.1 mm/s. The shape of the "flowing" part of this propagator is not simply a Gaussian-broadened step function, which would be the case for laminar flow in a single xylem vessel only (Eq. [7]). Apparently, the volume element corresponding to the pixel with the propagator shown in Fig. 6 contains more than one vessel with flowing water. It might hold a part of a second vessel with flowing water that causes more signal than expected in the lower displacements (10–20 μm) of the propagator.

DISCUSSION AND CONCLUSIONS

The amplitude images (Figs. 3a, 4a, and 5c) of the different objects show that the TSE part of the sequence produces real images without unexpected artifacts. This means that the amplitude and phase of the NMR signal throughout the echo train is constant, which is a prerequisite for calculating real images and for monitoring flow-induced phase shifts within the echo train.

The calculation of D of the stationary water in the six tubes of the first phantom by the fit of the propagator to a Gaussian function resulted in values around the value of D for free water at 24°C (Table 1). The error in D, which is 8% or smaller for tubes I to V, remains well within a standard deviation (SD) of 10%. Since D is proportional to $\mathbf{g}^2$ (Eq. [2]) and the gradient noise can be up to 3%, deviations in D up to 6% are the result of gradient noise.

The calculation of D by the Stejskal–Tanner (ST) analysis should result in approximately the same values for D as obtained with the propagator analysis, because the same data are used for both calculations. In the measurements reported here, the ST analysis gives less accurate results. In the propagator analysis three parameters are fitted to the data, which is one parameter more than in the ST analysis. This third parameter p, the position of the Gaussian-shaped propagator, is not always zero as can be seen in Fig. 4c. The ST analysis does not have a parameter to correct for this error, which, of course, is also present in the data before the FT, and this error results in a higher SD in D, despite the fact that introducing extra fit parameters normally results in higher SD values.

From the results in Fig. 3a one can see that the very short T_2 values cause a smearing of the signal intensities in the vertical, phase-encoding direction. The shape of the propagator of that volume element, however, remains the same as the propagator originating from the pixels with a longer T_2, though its total amplitude is smeared over the neighboring pixels. Tube VI of the first phantom is an example of a sample with volume elements with very short T_2 values (5.4 ms). The calculation of D by propagator analysis is still rather accurate, albeit with a higher SD. In homogeneous samples, this poses no problem. Problems can emerge if two neighboring volume elements both have a short T_2 and a different displacement behavior: in adjoining pixels of a TSE image the shape of the propagator is mainly defined by the displacement behavior of the corresponding volume element, but in this special case, both pixels will experience substantial interference from each other. One might consider lowering the spatial resolution to merge pixels with water with large and small T_2 values together. This could also be a strategy in quantifying the propagators of all pixels in a slice to calculate the total volume flow through the slice (*33*).

The second phantom shows that besides diffusion also flow information is well preserved in the echo train. An unstable amplitude and phase in the echo train would obscure any displacement-correlated phase shift, enforced by the PFGs. The measured maximum flow velocities (4.62 and 4.76 mm/s) are accurate within 2% to the actual maximum flow velocities in the tube, as driven by the pump (4.72 mm/s).

The areas with water transport in the xylem of a tomato plant emerge after constructing images at different positions on the displacement axis (Fig. 5d). These three areas can also be recognized in the T_2 image. In the T_2 image (Fig. 5b) the areas show a high T_2 variance, which may be caused by large differences in T_2 of the water in a xylem vessel and water of supporting or accompanying cells. One pixel can contain more

vessels with varying diameters than another, resulting in different T_2 values.

The shape of a propagator from a volume element in the xylem area is not a summation of a symmetrical Gaussian-shaped peak at zero displacement and one step function, broadened by diffusion. At the obtained resolution one pixel represents one or more xylem vessels and/or a part of one or more xylem vessels with accompanying tissue. This can result in a range of propagator shapes that are not known in advance and thus obstructs the possibility to fit the propagator to a model function for quantification. The possibility to obtain propagators with high spatial resolution, acceptable accuracy, and a realistic measurement time demands the need for a model-free quantification of the propagator formalism (*33*).

The pixel size and the amount of time spent on acquisition of the images of the tomato plant were small enough to justifiably entitle the PFG-TSE technique as a fast microscopic displacement imaging technique. If averaging is not necessary, and one would use 16 PFG steps, tr 1 s, tf 32, and image size 128×128, the acquisition of a complete set of propagator images would take 2 min 8 s. At 0.47 T an accurate map of water displacements in a tomato plant stem with a resolution of $117 \times 117 \times 3000$ μm could be obtained in 17 min 8 s.

ACKNOWLEDGMENTS

This research is financially supported by the EU Large Scale Facility WNMRC and the Technology Foundation (STW).

REFERENCES

1. T. W. J. Scheenen, D. van Dusschoten, P. A. de Jager, and H. Van As, *in* "Spatially Resolved Magnetic Resonance, Methods, Materials, Medicine, Biology, Rheology, Geology, Ecology, Hardware" (P. Blümler, B. Blümich, R. Botto, and E. Fukushima, Eds.), Vol. 1, pp. 481–486, Wiley-VCH, Weinheim, New York (1998).
2. P. T. Callaghan, C. D. Eccles, and Y. Xia, *J. Phys. E* **21,** 820–822 (1988).
3. P. T. Callaghan, W. Köckenberger, and J. M. Pope, *J. Magn. Reson., Ser. B* **104,** 183–188 (1994).
4. W. Köckenberger, J. M. Pope, Y. Xia, K. R. Jeffrey, E. Komor, and P. T. Callaghan, *Planta* **201,** 53–63 (1997).
5. E. Kuchenbrod, M. Landeck, F. Thürmer, A. Haase, and U. Zimmermann, *Bot. Acta* **109,** 184–186 (1996).
6. M. Rokitta, A. Peuke, U. Zimmerman, and A. Haase, *in* "ISMRM Book of Abstracts, Sydney," P1928 (1998).
7. P. Mansfield, *J. Phys. C: Solid State Phys.* **10,** L55 (1977).
8. P. Mansfield and L. Pykett, *J. Magn. Reson.* **29,** 355–373 (1978).
9. J. Hennig, A. Nauerth, and H. Friedburg, *Magn. Reson. Med.* **3,** 823–833 (1986).
10. C. F. Beaulieu, X. Zhou, G. P. Cofer, and G. A. Johnson, *Magn. Reson. Med.* **30,** 201–206 (1993).
11. E. O. Stejskal and J. E. Tanner, *J. Chem. Phys.* **42,** 288–292 (1965).
12. D. N. Firmin, R. H. Klipstein, G. L. Hounsfield, M. P. Paley, D. B. Longmore, S. R. Underwood, and R. S. Rees, *Magn. Reson. Med.* **12,** 316–327 (1989).
13. D. N. Firmin, G. L. Nayler, P. J. Kilner, and D. B. Longmore, *Magn. Reson. Med.* **14,** 230–241 (1990).
14. J. E. M. Snaar and H. Van As, *J. Magn. Reson.* **87,** 132–140 (1990).
15. D. N. Guilfoyle, P. Gibbs, R. J. Ordidge, and P. Mansfield, *Magn. Reson. Med.* **18,** 1–8 (1991).
16. Y. Xia and P. T. Callaghan, *Magn. Reson. Med.* **23,** 138–153 (1992).
17. H. Van As and D. van Dusschoten, *Geoderma* **80,** 389–403 (1997).
18. J. Kärger and W. Heink, *J. Magn. Reson.* **51,** 1–7 (1983).
19. D. van Dusschoten, C. T. Moonen, P. A. de Jager, and H. Van As, *Magn. Reson. Med.* **36,** 907–913 (1996).
20. D. van Dusschoten, P. A. de Jager, and H. Van As, *J. Magn. Reson. Ser. A* **116,** 237–240 (1995).
21. M. D. King, J. Houseman, S. A. Roussel, N. Van Bruggen, S. R. Williams, and D. G. Gadian, *Magn. Reson. Med.* **32,** 707–713 (1994).
22. F. Schick, *Magn. Reson. Med.* **38,** 638–644 (1997).
23. H. T. Edzes, D. van Dusschoten, and H. Van As, *Magn. Reson. Imag.* **16,** 185–196 (1998).
24. C. J. Rofe, J. Van Noort, P. J. Back, and P. T. Callaghan, *J. Magn. Reson.* **108,** 125–136 (1995).
25. P. T. Callaghan, *J. Magn. Reson.* **87,** 304–318 (1990).
26. M. T. Vlaardingerbroek and J. A. den Boer, *in* "Magnetic Resonance Imaging," Vol. 1, pp. 115–166, Springer-Verlag, Berlin (1996).
27. M. L. Glyngell, *Magn. Reson. Imag.* **6,** 415–419 (1988).
28. T. Loenneker, F. Hennel, and J. Hennig, *Magn. Reson. Med.* **35,** 870–874 (1996).
29. C.-N. Chen and D. I. Hoult, "Biomedical Magnetic Resonance Technology," Medical Science Series 340, IOP Publishing Ltd., Bristol, New York (1989).
30. W. T. Vetterling, S. A. Teukolsky, W. H. Press, and B. P. Flannery, *in* "Numerical Recipes Example Book (C)," 247, Cambridge Univ. Press, Cambridge, UK (1992).
31. P. A. de Jager, F. J. Vergeldt, and H. Van As, *in* "Book of Abstracts, 14th EENC," 211, Bled, Slovenia (1998).
32. C. van der Schoot, "Determinants of Xylem-to-Phloem Transfer in Tomato," Thesis, Utrecht University, Utrecht (1989).
33. T. W. J. Scheenen, D. van Dusschoten, P. A. de Jager, and H. Van As, *in* "ISMRM Book of Abstracts, Philadelphia," P2005 (1999).